RESEARCH ARTICLE

Key Points:
- Dust storms' influence is strongest in the thermosphere-ionosphere source region
- Hypothesize a dust opacity threshold for a long-lived effect on the ionosphere

Correspondence to:
S. Xu,
xussui@umich.edu

Mars photoelectron energy and pitch angle dependence on intense lower atmospheric dust storms

Shaosui Xu[1], Michael W. Liemohn[1], David L. Mitchell[2], and Michael D. Smith[3]

[1]Department of Atmospheric, Oceanic, and Space Sciences, University of Michigan, Ann Arbor, Michigan, USA, [2]Space Sciences Laboratory, University of California, Berkeley, California, USA, [3]NASA Goddard Spaceflight Center, Greenbelt, Maryland, USA

Abstract We have conducted a survey of the Mars Global Surveyor (MGS) electron data across all the pitch angles of 12 usable energy bins (11–746 eV) for dayside photoelectron observations over regions of strong crustal fields. Studies have shown that solar EUV flux is the main controlling factor, but dust storms play an important role as well. Our study of different energies and pitch angles has shown that the unusual bimodal solar flux dependence is not a common feature but mainly found in low energies and a few bins of higher-energy channels. By multiplying time-history dust opacity with a solar EUV proxy as a new controlling function, the statistically significant increase of the correlation of photoelectron flux against this function indicates that dust storms have a long-lasting influence on high-altitude photoelectron fluxes, especially at low energies and the pitch angle source regions of high-energy channels. The correlation increases experienced by the pitch angle source regions of all examined energy channels suggest that dust storms' influence most likely happens in the thermosphere-ionosphere source region of the photoelectrons, rather than at exospheric altitudes at or above MGS. Furthermore, by isolating the global-scale dust storm in Mars year 25 (2001) from the rest, the results suggest that this storm is entirely responsible for the second solar flux-dependent trend. While not excluding the possibility of this phenomenon being a one-time event, we hypothesize that there is a threshold of dust opacity at which the low-altitude dust's influence on high-altitude photoelectron fluxes begins to be significant.

1. Introduction

By analyzing dayside photoelectron observations of the magnetometer/electron reflectometer (MAG/ER) from Mars Global Surveyor [*Acuña et al.*, 1992; *Mitchell et al.*, 2001] over regions of strong crustal fields, *Trantham et al.* [2011] quantitatively determined that among all possible candidates, the local solar EUV proxy was the main controlling factor of photoelectron fluxes. In spite of the normal linear dependence between these two, a second linear trend is, however, found, with the primary contribution being the especially higher-photoelectron fluxes from late 2001 to early 2002 (late Mars year 25 to early Mars year 26).

This time period corresponds to a global-scale dust storm at Mars year (MY) 25 [e.g., *Smith et al.*, 2002; *Clancy et al.*, 2010]. Most of Mars' large dust storms occur in southern springs and summers, when Mars is near perihelion. Dust suspended in the dry Martian atmosphere is known to play an important role in the Martian atmospheric dynamics; when dust opacity is high enough, its absorption of solar radiation is comparable to CO_2 gas, thus contributing to the variability of the circulation and weather on Mars [e.g., *Gierasch and Goody*, 1972; *Haberle et al.*, 1982; *Medvedev et al.*, 2011].

Even though the dust remains below 60 km, its influence extends to higher altitudes as it absorbs solar radiation and heats the atmosphere, causing an elevated atmospheric density at higher altitudes due to the increased scale height. Many studies have been conducted on dust storm influences on the Martian upper atmosphere [e.g., *Keating et al.*, 1998; *Bougher et al.*, 1999, 2004, 2006; *Baird et al.*, 2007; *Lillis et al.*, 2008, 2010a; *England and Lillis*, 2012; *Withers and Pratt*, 2013]. The change in neutral atmosphere, especially the increase of neutral density due to a heated atmosphere caused by dust storms, leads to the variability of the ionosphere. On one hand, observations of MGS, both during aerobraking [*Keating et al.*, 1998] and during the science phasing orbits [*Tracadas et al.*, 2001], have shown a factor of 3 increase in the mass density at 130 km altitude and a factor of 2 increase at 180 km a few days after the start of dust storms, respectively. By examining a few different dust storm events, *Withers and Pratt* [2013] found that the increases of upper atmospheric density were usually a factor of a few responding to moderate regional storms and of an order

of magnitude during the large storms. On the other hand, modeling results of *Bougher et al.* [1997] on a 20 Martian solar days dust storm also showed a 5–10 times increase of thermospheric density at 110 km; furthermore, *Bell et al.* [2007] conducted a sensitivity study of the vertical depth of the dust layer and found, when the 9 μm dust optical depth $\tau = 0.3$, a 100% increase in atmospheric density at the equatorial height of 110 km and a 650% increase at the winter pole. In fact, the study of *Bell et al.* [2007] implies that the Hadley circulation transmits changes in the lower atmosphere caused by dust loading into the upper atmosphere, which is supported by the study of *Withers and Pratt* [2013]. Neutral density is one of the dominant controlling factors of the ionosphere electron density profile (with similar effects expected on ionospheric photoelectrons). Increased altitudes of the ionospheric peak electron density due to the expanded atmosphere during dust storms have been observed [*Hantsch and Bauer*, 1990; *Wang and Nielsen*, 2003]. In fact, the height of the electron peak can also be used to study the physical state of the Mars lower and upper atmosphere [*Bougher et al.*, 2004; *Zou et al.*, 2011].

MGS was operated at altitudes around 400 km, well above the electron peak altitude. Using accelerometer data from this satellite, *Forbes et al.* [2008] concluded that the dust storm at MY 25 seemed to not influence exospheric temperature or density, but the authors only addressed the relationship between the instantaneous dust opacity within $\pm 30°$ latitude and the exosphere. *Liemohn et al.* [2012], however, conducted the time-history influence of dust storms on dayside photoelectrons observed by MGS above the strong crustal fields. The inclusion of seven Earth month time-history dust opacity not only successfully merged two linear EUV dependence trends into one but also significantly increased the correlation of photoelectron fluxes and the new controlling function, EUV proxy multiplying time-history dust opacity. This modification to the controlling function, sometimes corrected by an order of magnitude, can be considered as change to the photoelectron production rate and/or to high-altitude scattering effects, which can be caused by the change in the neutral density at ionospheric altitudes and/or at exospheric altitudes, respectively.

Since both *Trantham et al.* [2011] and *Liemohn et al.* [2012] only investigated one single velocity space bin, 27 eV at pitch angle 80°–90°, it is necessary to examine dust storms' effects on all the available energy channels and pitch angles. This examination allows us to investigate the physical processes behind the dust storms, which the former two studies barely addressed. Differences in the response of different energy photoelectrons may be an indicator of physical processes that have an energy preference, such as scattering and/or collisions. The pitch angle can give information on where photoelectrons reside, for example, photoelectrons near 90° pitch angle are mostly located and bouncing at or beyond the MGS orbit. The examination of pitch angle bins might hint where those dust-related physical processes most likely happen.

2. Methodology

Acuña et al. [1992] has given the detailed description of the MAG/ER instrument on board MGS. Our study focuses on dayside photoelectrons, and the data set is obtained similar to the methodology of *Trantham et al.* [2011]. Photoelectrons observed at an altitude of 400 km by MGS on closed magnetic field lines are most likely originated from the ionosphere lower down on that same field line. On Mars, a region consisting of closed magnetic loops is mostly within longitudes of 160° and 200° and north latitudes of −30° and −70°, and this spatial constraint is applied to our data selection, along with a magnetic field magnitude minimum constraint (35 nT). In addition, to avoid cusps between loops where solar wind electron precipitation could happen, only elevation angles within $\pm 45°$ of horizontal are selected. All energies were intended to be examined, but the photoelectron fluxes in energy channels higher than 746 eV are at or near the one-count instrument threshold. Hence, only 12 out of the 19 energy channels are examined, from 11.4 to 746 eV (lower bound of the lowest channel and upper bound of the highest channel, respectively). Also, a pitch angle bin size of 10° is used, mapping the ER anode sectors into these 18 identically sized pitch angle bins.

However, our full examination of all available energy and pitch angle bins found that the method above is insufficient. Figure 1 shows an example of one selected orbit, Earth year 2000 Day 288, 14:29:01. Figures 1a and 1f show how the magnetic elevation angles and latitudes change within this 490 s interval, respectively. The latitude is from −60° to −35°, crossing most of the entire spatial box of strong crustal fields, while the B elevation angle increases from −35° to 45°, decreases to −45°, and then increases to 45° again. The smooth change of B elevation angle indicates the loop structure of the magnetic field. The data absent from 120 s to 200 s are due to the elevation angle criteria described above. Other large gaps are caused by the unsuccessful conversion from anode bins into pitch angles. The eight contour plots in Figure 1 show fluxes of
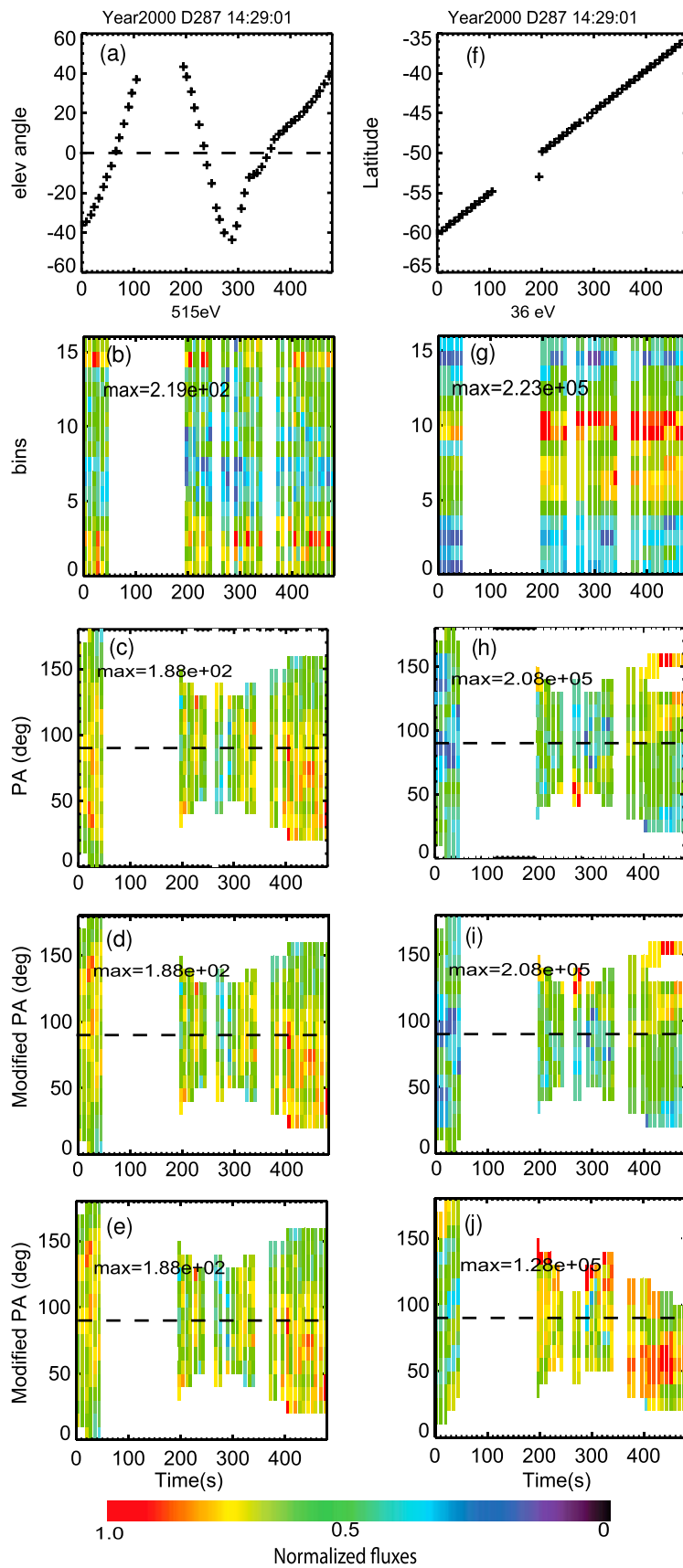
Figure 1

two energy channels, 515 eV (Figures 1b–1e) and 36 eV (Figures 1g–1j). Figures 1b and 1g are the differential electron fluxes recorded in the 16 anode sectors against time for two energies, respectively, while the color is normalized electron flux (relative to the maximum value, also given in each plot) for all eight contour plots. Here since the time for each measurement from MAG/ER is different, a 6 s time interval is used in the contour plots, causing the small gaps in between data points. The ER has a 360° × 14° field of view (FOV) and measures each pitch angle (PA) twice, once for each 180° span of instrument azimuth around the FOV. Pitch angles are determined by the magnetic field's azimuthal and elevation angles and also the azimuth of the incident electron, i.e., the angle of each sector in the FOV plane [*Mitchell et al.*, 2001]. Figure 1g shows constant high fluxes across sectors 5–12, regardless of the elevation angle of the magnetic field and the latitude of the measurement. In fact, this feature is found in energies lower than 53 eV for almost the entire 7 year data. Given the fact that these eight sectors look toward and along the spacecraft bus, the systematically higher flux values of these sectors at lower energies throughout this interval of changing magnetic field direction strongly suggest contamination by spacecraft photoelectrons and secondary electrons.

Originally, simply averaging the fluxes of two bins of the same pitch angle for all energies is used, shown in Figures 1c, 1d, 1h, and 1i. Because of this new discovery of contamination at low energies, while the same method is used for energies higher than 53 eV, only the rest of the eight sectors other than sectors 5–12 are taken into account to calculate the electron fluxes of lower energy channels, shown in Figures 1e and 1j. Notice that for Figures 1e, 1d, 1i, and 1j with time along the *x* axis, the *y* axis is now denoted as "Modified PA." Aside from converting fluxes of 16 sectors into pitch angle distributions (PADs), the pitch angle is also flipped when the B field points downward (data points below the dashed line in Figure 1a). For example, if B points toward the planet, the original pitch angle of 10° would now be 170°. In other words, electrons at pitch angle 0°–90° (90°–180°) always have a velocity component away from (toward) planet. Figures 1c and 1d (also Figures 1h and 1i) show a comparison between the normal PA and "Modified PA." In this case, we can separate pitch angles into three parts. For PA near 90°, it is the so-called trapped zone since electrons are mostly scattered into these pitch angles due to their source (ionosphere) being located at altitudes of strong magnetic field and then bounce at MGS altitudes or above. As magnetic loops of strong crustal fields are relatively short, photoelectrons basically come from the ionosphere at one end of the loop, then move along the field line, and are lost to the ionosphere at the conjugate end of the field line, if they are not scattered. As a result, upward electrons, especially PA near 0°, can be considered as fresh photoelectrons coming from the ionosphere while downward electrons (PA near 180°) are those moving along the field lines and toward the sink, far away from their source region.

After applying the contamination filter, the unfiltered Figure 1d is identical to the filtered Figure 1e since the filter has no effect on energy channels higher than 53 eV. However, for 36 eV, Figure 1i has fewer bins than Figure 1j because the contamination filter removes some of the data in the pitch angle space. Pitch angles greater than 120° after 350 s, where fluxes are especially high, are absent because fewer sectors are used to determine PADs for low-energy channels. At the meantime, the maximum of Figure 1j now is 60% of Figure 1i with the removal of those high fluxes. As a result, PADs are now more isotropic.

To further confirm that the method above is valid, example energy spectra are shown in Figure 2. The three plots correspond to three pitch angle bins, 0°–10°, 80°–90°, and 170°–180°, respectively, at the same time period as Figure 1. The energy spectrum of every single time is overplotted, highlighted in different colors, black for 0 s and then green and then red for the latest time, 490 s. Because ER only provides 2-D samples of electron fluxes, 90° pitch angle is constantly measured while more field-aligned pitch angles are sampled only part of the time. As a result, only three to five spectra are seen in Figures 2a and 2c while more are seen in Figure 2b. Nevertheless, clear photoelectron energy spectrum features, such as the knee at 60–70 eV, the sharp drop at around 500 eV, and the cutoff at 800 eV [e.g., *Mitchell et al.*, 2001; *Liemohn et al.*, 2003], are seen in Figure 2. The absence of the low-energy part in Figure 2a is due to the spacecraft photoelectron

Figure 1. An example of one selected orbit, Earth year 2000 Day 288, 14:29:01. (a, f) How the magnetic elevation angles and latitudes change within 490 s, respectively. (b–e) Energy channel 515 eV. (g–j) Energy channel 36 eV. The color is normalized electron flux (relative to the maximum value (cm^{-2} s^{-1} $ster^{-1}$ eV^{-1}) of each plot). Figures 1b and 1g are the differential electron fluxes recorded in the 16 anode sectors against time, while Figures 1c and 1h are the fluxes converted into pitch angle distributions (PADs). Figures 1d, 1e, 1i, and 1j are fluxes converted into PADs but with Modified PA bins as the *y* axis. The dashed line in Figure 1a marks 0 magnetic elevation angle, below which the pitch angle is flipped. The dash line in Figures 1c–1e and 1h–1j marks 90° pitch angle.
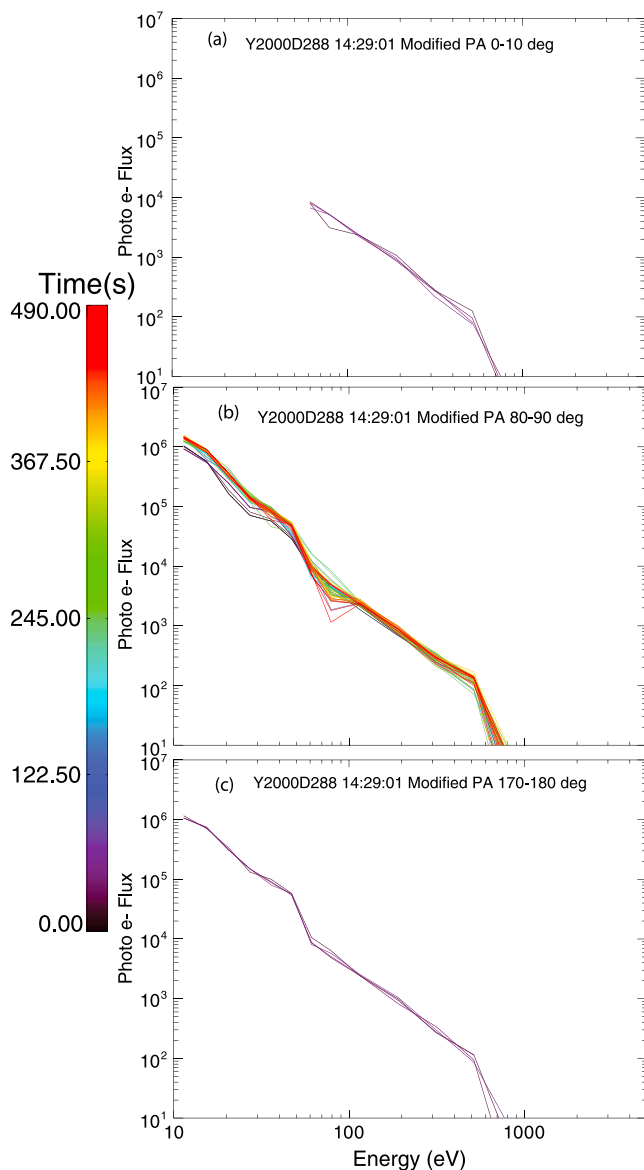
Figure 2. Energy spectra of differential number fluxes (cm^{-2} s^{-1} ster^{-1} eV^{-1}) at three different pitch angles: (a) 0°–10°, (b) 80°–90°, and (c) 170°–180°. Colors highlight different data points within the same time period as Figure 1.

contamination issue described above, resulting in fewer sectors used to calculate low-energy photoelectron fluxes.

The Thermal Emission Spectrometer (TES) instrument on MGS is fully described by *Christensen et al.* [1992, 2001], and the details of extracting dust opacity values from these observations are given by *Smith* [2004]. The dust opacity record shows a clear seasonal variation, with higher values caused by dust storms occurring each southern hemisphere spring and summer. Since even local dust events can cause a global response of the upper atmosphere [e.g., *England and Lillis*, 2012; *Withers and Pratt*, 2013], this study is based on the globally averaged dust opacity values. The dust opacities at MGS' latitude were presented by *Liemohn et al.* [2012] and other studies.

To investigate time-history effects of dust storms, time series of various quantities are shown in Figure 3. Figure 3a presents photoelectron fluxes of 36 eV at pitch angle 0°–10° against time. The blue/red dots are the data values, and the black vertical lines give the mean and 3σ uncertainty with a bin size of 0.1 Earth year (approximately 37 Earth days). The red dots are highlighted as the time period of the global dust storm in MY 25 and exhibit the second linear dependence on the solar EUV proxy, while the blue dots are for the rest of "normal" time period. Here the 3σ uncertainty is used to exclude extremely high fluxes, along with the unusual high fluxes at the beginning

of year 1999 (approximately the first 73 days of year 1999). Though consisting of a small amount of data points, these high fluxes can cause big drops of the Pearson correlation coefficients. To justify this exclusion, first, the energy spectra of the unusual high fluxes at the beginning of year 1999 clearly show that these electrons are not photoelectrons. Second, these high fluxes can be magnetosheath fluxes. Third, the solar EUV proxy might be more of a representative of an average photoelectron fluxes. Finally, this study focuses on the two main linear trends dependence on the solar EUV proxy, and these excluded fluxes are just a small portion of the data set. The exclusion of these fluxes should barely affect the findings of this study. Figure 3e is the local EUV proxy, i.e., $F_{10.7}$ cm solar flux at Mars multiplying a solar zenith angle-dependent Chapman function [*Trantham et al.*, 2011], against time. The very low values during southern summer [*Liemohn et al.*, 2012, Figure 1c], when the crustal fields were at LT 2 A.M. but partially illuminated due to the tilt of the planet, are also excluded as the partially illuminated magnetic loops very likely straddle the terminator, and therefore, these fluxes may behave differently. Figures 3b–3d are time-history dust opacity values against
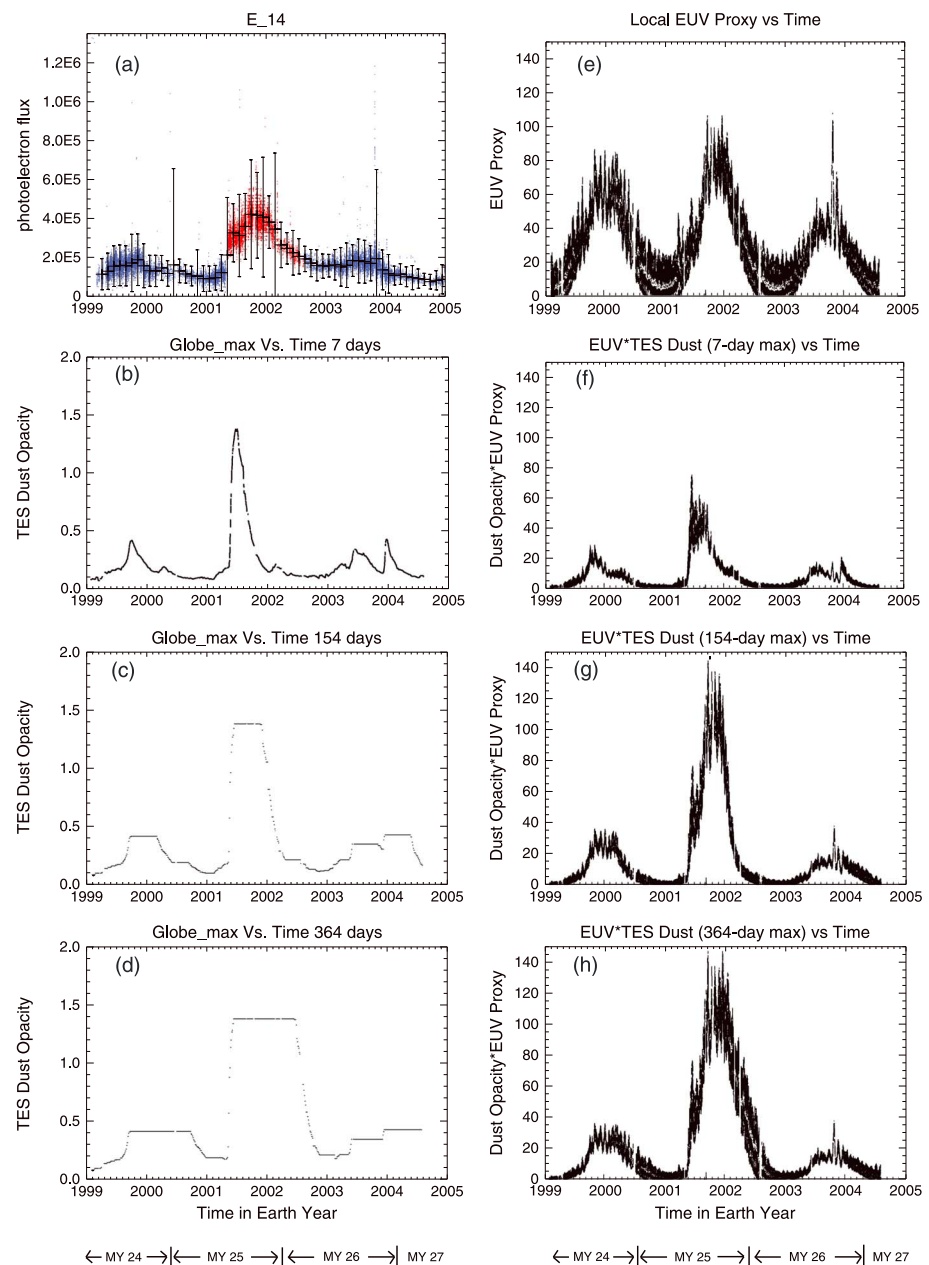
Figure 3. (a) Photoelectron fluxes (cm^{-2} s^{-1} ster^{-1} eV^{-1}) at 36 eV and pitch angle 0°–10° against time. The black vertical lines give the mean and 3σ uncertainty of all of the individual red/blue data points within a bin size of 0.1 Earth year. (b–d) 7, 154, and 354 Earth day time-history dust opacity values against time, respectively. (e) The local EUV proxy. (f–h) The new controlling functions, using the local EUV proxy at Mars shown in Figure 3e multiplied by the dust opacity values in Figures 3b–3d, against time.

time. *Liemohn et al.* [2012] came up with two different methods to determine dust storms' long-term effects, time-history averages, and maximums of dust opacities within a certain time window. In other words, for a data point, tracing back across a specified time length, either the averaged dust opacity or maximum within this window will be the new value. Here time-history maximums are shown as examples, and the window lengths are 7 Earth days, 154 Earth days, and 354 Earth days, respectively. Figures 3f–3h are the new controlling functions, calculated as the EUV proxy at Mars (Figure 3e) multiplying the left three corresponding time-history maximum dust opacities, against time. As said above, this inclusion of the time-history dust opacities serves as a modification to the dominant factor, solar EUV, of photoelectron fluxes. For instance,
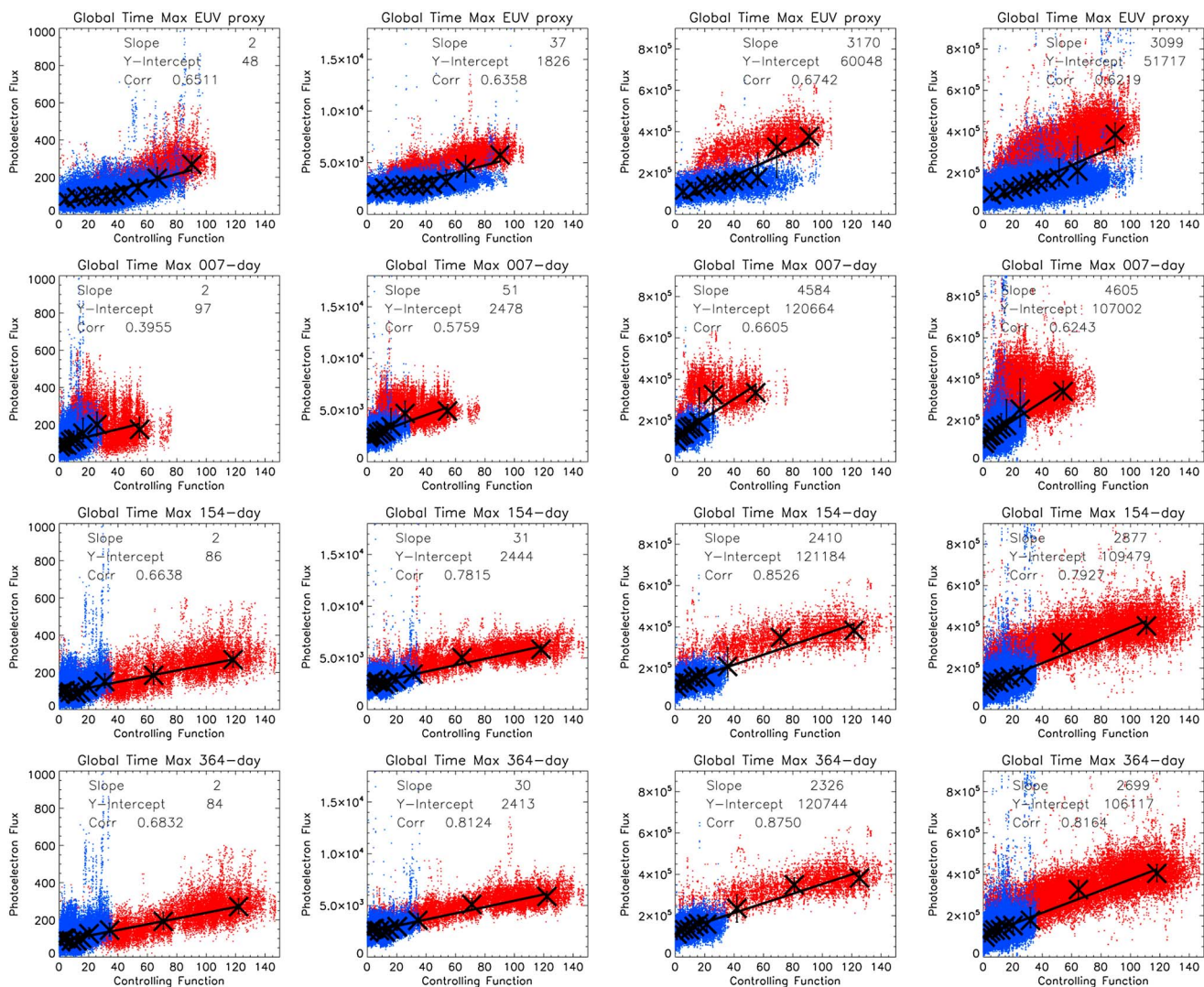
Figure 4. The four columns correspond to the scatterplots of the photoelectron fluxes (cm^{-2} s^{-1} ster^{-1} eV^{-1}) of 515 eV at 0°–10°, 116 eV at 0°–10°, 36 eV at 0°–10°, and 36 eV at 80°–90°, respectively, against different controlling functions. The x axis for each row is EUV proxy, EUV proxy multiplying 7 day, 154 day, and 364 day time-history dust opacity, corresponding to Figures 3e–3h. The asterisks in each panel mark the median values and quartiles (as error bars) for 10 bins with equal data points inside (with slope, intercept, and correlation coefficient given in the upper). In addition, data points are highlighted in red and blue, the same as Figure 3a, with red for especially high flux from Earth year late 2001 to early 2002 while blue for the rest of time.

the multiplication of a high dust opacity may imply a denser neutral atmosphere at ionospheric altitudes and/or a higher collision rate due to a denser exosphere. Comparing Figures 3f–3h with 3e shows that this adjustment sometimes exceeds an order of magnitude change in the controlling function values.

3. Results

With the new controlling functions, the study of the relationship between dayside photoelectron fluxes and TES dust opacities is conducted in section 3.1. To further investigate the specialness of the global-scale dust storm at MY 25, two sets of modified dust opacities are also applied to the same method, with the results shown in section 3.2.

3.1. Relationship With TES Dust Opacities

Figure 4 shows the scatterplots of the fluxes of photoelectrons of different energies and different pitch angles (PAs) against various controlling functions. The first three columns are photoelectrons of 515 eV, 116 eV, and 36 eV at PA 0°–10°, and the fourth shows 36 eV at PA 80°–90°. The x axis for each row is EUV proxy, EUV proxy multiplying 7 day, 154 day, and 364 day maximum time-history dust opacity. In each panel

of Figure 4, all the data points are divided into 10 bins with equal number of data points inside each bin. Then the median values and quartiles (as error bars) for each bin are marked with the asterisks, with a linear fit to these median values shown as a black line. The slope and intercept quantities to this fit, along with the Pearson correlation coefficients of all the data points in each plot, are also given in each panel. In addition, data points are highlighted in red and blue, the same as Figure 3a, with red designating the especially high-flux interval from Earth year late 2001 to early 2002 (late MY 25 to early MY 26), while blue is used for the rest of the time.

The scatterplots of photoelectron fluxes against EUV proxy only (the first row) show a separation of photoelectron fluxes in the last three columns, the same feature as found in *Trantham et al.* [2011]. In fact, this separation has been seen in 8 (×18 pitch angle bins) out of 12 energy bins with four energy channels as exceptions: 515 eV, 313 eV, 79 eV, and 61 eV. For example, the top plot of the first column, 515 eV, does not show a clear separation. On one hand, the results demonstrate that this double linear trend is not exclusive for only 27 eV photoelectrons at PA 80°–90° [*Trantham et al.*, 2011] but is a common feature of the majority of energy and pitch angle bins. Especially, the fact that this feature exists in source cone pitch angles hints that the driving processes tend to happen at the source, i.e., the thermosphere/ionosphere, since photoelectrons in the trapped pitch angles are less likely to affect those in the source regions. An example of a different pitch angle, 80°–90°, is also shown in the last column. Usually, the scatterplots of pitch angle near 90° appear to be broader in flux than for field-aligned PA bins, which either can be a result of more data sampled at these particular pitch angles due to the design of the instrument or indicates some underlying physical processes. On the other hand, this feature is not found in every energy and pitch angle bin. In fact, the existence of these exceptions makes the question more complicated. While the possibility that this feature has an energy preference cannot be completely excluded, it is more likely that the exception of 79 eV and 61 eV is due to spacecraft potential. These two energy bins happen to be near the knee of the photoelectron energy spectrum [e.g., *Mitchell et al.*, 2001; *Liemohn et al.*, 2003], where there is an order or so of magnitude decrease of flux from 50 eV to 70 eV. The energy shift caused by spacecraft potential might cause the large variation of the fluxes of these two energies. As for the other two high-energy channels that do not show the double-linear trend, 515 eV and 313 eV, it is probably because the driving factor of this feature does not favor these high-energy photoelectrons.

The separation of the photoelectron population into two distinct linear trends with respect to the local EUV proxy suggests the existence of another controlling factor of photoelectrons. *Trantham et al.* [2011] investigated a few other possible candidates including solar wind pressure, the magnitude, and elevation angle of magnetic field, as well as longitude and latitude (with one velocity space bin, 27 eV at PA 80°–90°) but concluded that these candidates have little control of photoelectrons. Our similar investigation on the rest of the energy and pitch angle bins seems to support this conclusion, as shown in the first row of Figure 4 for a few examples and checked for all others. However, *Liemohn et al.* [2012] provided another candidate, dust storms, and demonstrated that global dust storms may be responsible for the particularly high fluxes at Earth year 2002 by using a multiple of EUV and dust opacity as a new controlling function. Also, the correlation is the best with the use of a time-history of globally averaged dust opacity value instead of the instantaneous value, which indicates a long-term influence from dust storms. However, this research also focuses on only one bin, 27 eV at PA 80°–90°.

The results above demonstrate that different energies may have different responses; hence, it is necessary to investigate dust storms' influence on all energy and pitch angle bins. The same method as *Liemohn et al.* [2012] is applied to all usable bins. A few examples are also shown in Figure 4. The controlling function of rows 2 to 4 have multiplied three different time-history windows of dust opacity with local EUV proxy: 7 Earth days (1 week), 154 Earth days (5 months), and 364 Earth days (1 year), respectively. The controlling functions against time are shown in Figures 3e–3h, respectively. The second row sometimes has slightly better correlations compared to row one (such as 36 eV), but sometimes worse (such as 115 eV), and the separation has not yet disappeared. However, when the time-history window reaches 154 Earth days, the photoelectron fluxes against this controlling function are now one single linear trend, shown in row three. As the window runs longer to 364 Earth days the last three columns in the fourth row now have an even better linear trend. Rows two to four actually display the progress from two linear trends into a single one as the time-history window runs longer, if a separation is present in row one (EUV proxy only). The multiplication of a 5 month window dust opacity is able to successfully merge the separations. Mathematically, the Pearson correlation coefficient (*R*) (shown in the upper left corner of each panel) has a ~ 0.2 increase for the last
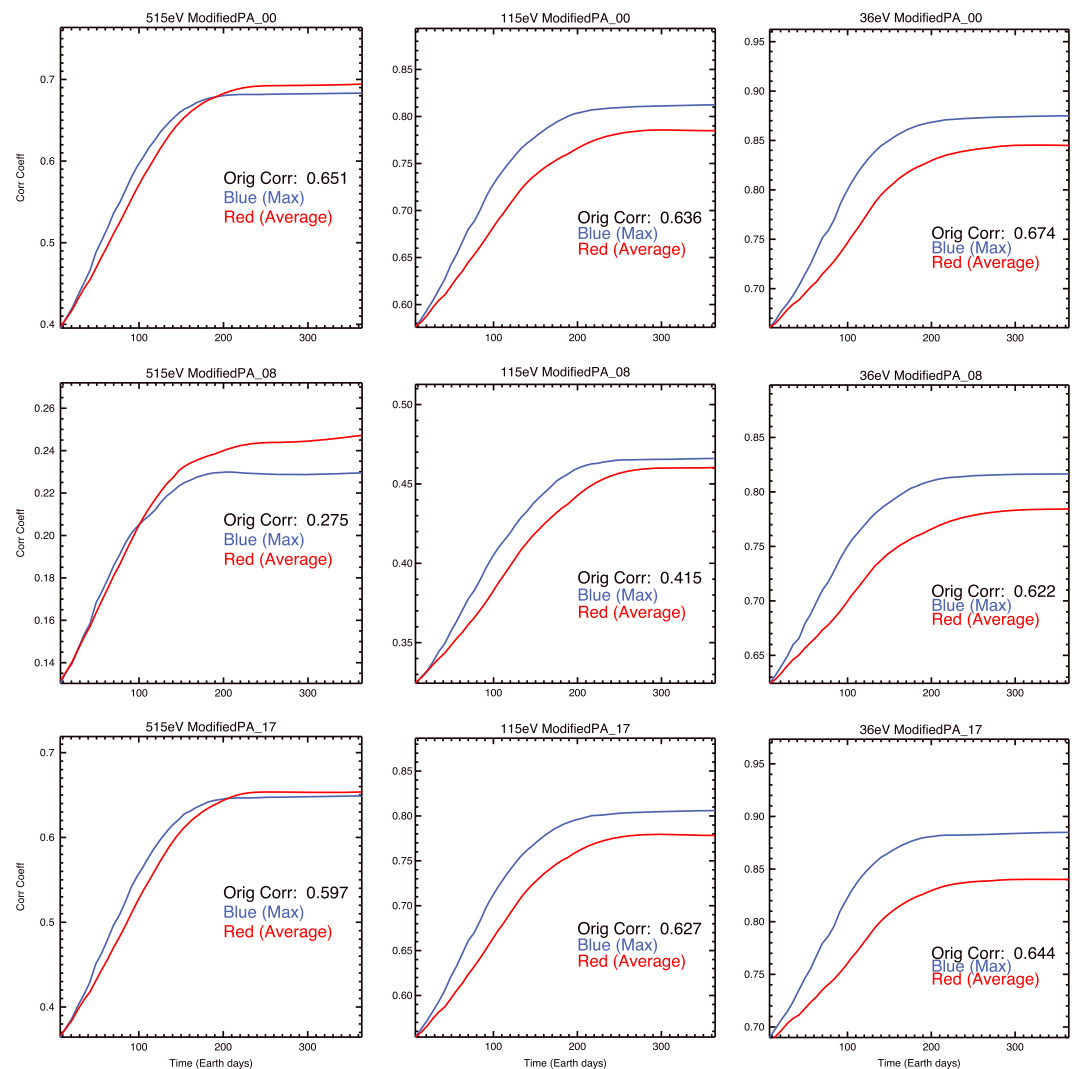
Figure 5. Correlation coefficient of photoelectron fluxes versus a controlling function (Figure 3g), with red and blue curves corresponding to a running-average time-history dust opacity method and a maximum-value time-history dust opacity method. "Orig Corr" denotes the correlation without the inclusion of dust opacities. The three columns are for three energy bins: 515 eV, 115 eV, and 36 eV and each row for different pitch angle bins: PA 0°–10°, PA 80°–90°, and PA 170°–180°, respectively. Notice that the y axes have different ranges for each plot.

two rows, compared to the first two rows. This increase is statistically significant, given the number of data points included to calculate the correlation, which is hundreds of thousands.

Notice that for each column in Figure 4, the correlation coefficients of the 154 Earth day time-history window and 364 Earth day window are almost the same, which indicates that R does not always rapidly increase as the time window increases. How R changes as a function of the time-history window is shown in Figure 5. The three columns are for three energy bins: 515 eV, 115 eV, and 36 eV and each row for different pitch angle bins: PA 0°–10°, PA 80°–90°, and PA 170°–180°, respectively. Notice that the y axes have different ranges for each plot. Two lines (red and blue) correspond to two methods to obtain the time-history dust opacity (the maximum and average within the window). A common feature of all the panels in Figure 5 (also seen in the rest of the pitch angle and energy bins not shown here) is that the correlation coefficient rapidly increases at first and then levels out for the rest of the time window.

However, in spite of the fact that rapid increases in the correlation are observed in all the energy and pitch angle bins as the time-history window increases, it is important to compare with the correlation with solar
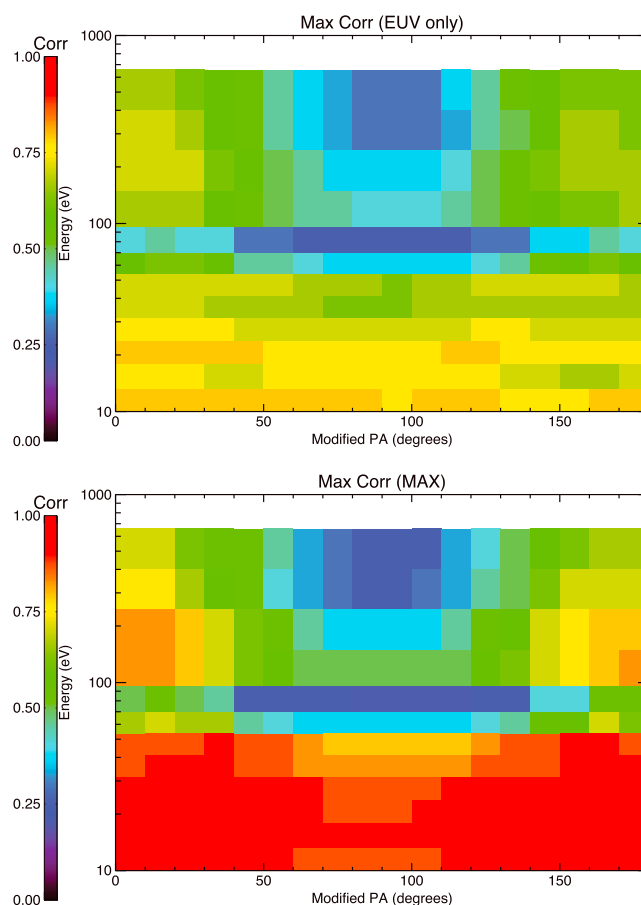
Figure 6. The correlation coefficients of the photoelectron fluxes versus a controlling function of all the energy and pitch angle bins. The controlling functions (top) local EUV proxy only and (bottom) local EUV proxy multiplied by the maximum-value time-history dust opacities.

EUV proxy only, denoted as "Orig Corr" in the right bottom corner of each panel. In fact, those energy and pitch angle bins that exhibited little to no separation of photoelectron fluxes in the scatterplots barely have any increase of correlation with window duration, especially in the trapped zone, such as 515 eV, PA 80°–90°. In this case, dust storms seem to have little effect on these energy channels. In contrast, the source region (pitch angle near 0° or 180°) of energy channels higher than 53 eV and all the pitch angles below 53 eV have shown a higher correlation than that of solar EUV proxy only. A few examples are shown in Figure 5. The increase is around 0.05 for 515 eV at both pitch angle bin 0°–10° and 170°–180° and 115 eV at PA 80°–90°. An increase of above 0.15 is seen in the source region of 115 eV and all three different pitch angles of 36 eV.

For those bins with higher correlation with inclusion of time-history dust opacities, the rapid increase of correlation stops at 120 Earth days (approximately 63° solar longitude (Ls)) or longer, which implies that the influence of dust storms is most likely long-lasting. After this point in the window duration setting, the change of R is within 0.01 as the time-history window runs longer. This level-off implies the lack of sensitivity toward the exact length of this time-history window, pointed out by *Liemohn et al.* [2012]. Also, because of the fact that the line shape of using the running average within a time-history window is similar to that of using the maximum value and that the latter usually has a similar or higher correlation than the former, especially for low energies, all the discussion below will be based on results of using this maximum value.

Two kinds of information can be extracted from Figure 5, the length of the time-history window and the improved correlation coefficients. For the former one, because of the insensitivity toward exact peak in the time-history window, the transition point, where R changes from a rapid increase to almost a constant, can be considered as a reasonable representative of this time length. Here two criteria are applied to determine this transition point. If dy is the subtraction of the maximum and minimum correlations, i.e., the correlation range of each panel of Figure 5, a transition point is such that its correlation is no more than $0.1 \times$ dy lower than the maximum correlation, defining a region near the maximum value, and also that its correlation is $\leq 0.05 \times$ dy larger than the previous point's correlation, to guarantee a very slow increase. In addition, since R is almost the same after this transition point, the correlation coefficient of this time point will be used as the improved correlation for the following discussion.

The correlation coefficients of all energy and pitch angle bins for both the case of the EUV proxy only and the case of including time-history dust opacities are given in Figure 6 (top and bottom), respectively. In Figure 6 (top), for energy greater than 53 eV, the correlations are mostly above 0.5 in the source region and lower in the trapped zone, especially low for all pitch angles of 79 eV, which is near the knee of the
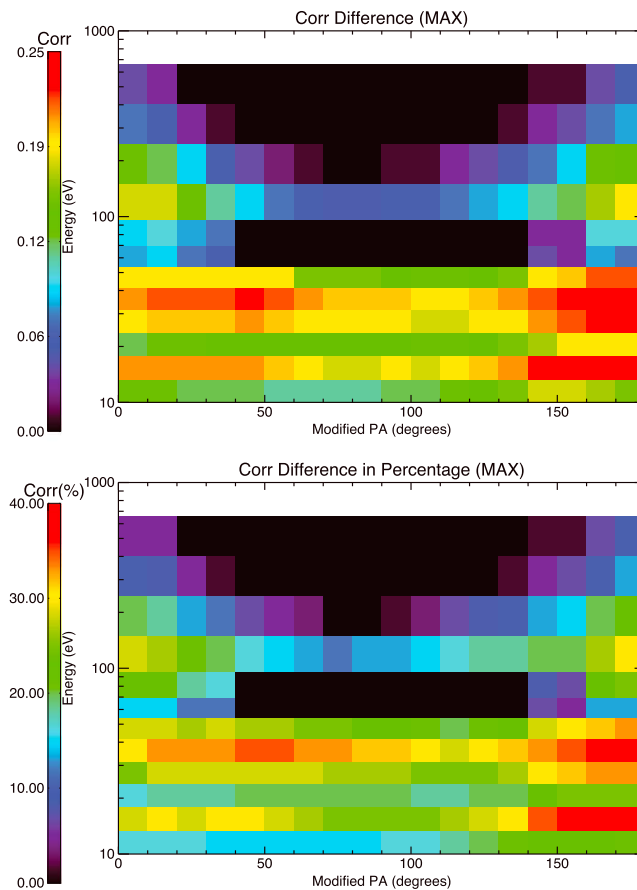
Figure 7. The (top) absolute and (bottom) relative correlation difference of Figure 6 (top and bottom). Note that the color scale for Figure 7 (top) is 0–0.2 while for Figure 7 (bottom) it is 0–40%.

photoelectron energy spectrum. For energy lower than 53 eV, the correlations are generally higher than 0.6, and not obviously lower in the trapped zone.

There are two possible reason for the slightly lower correlations at high energies. First, high-energy photoelectrons are produced by shortwave photons, such as X-rays, while the EUV proxy used here, based on $F_{10.7}$, is not a very good approximation for such shortwave solar flux. Second, the method used to account for the different angles of Mars and Earth are not able to capture all the solar flares and/or other short-lived solar activities. Another feature is that correlations of the trapped zone are lower for high energies. Notice that the measurement of MGS is at around 400 km, well above the source region of these examined photoelectrons (which is usually located below 200 km). Particles of pitch angles near 90° are mostly scattered into and reside at high altitudes. Their fluxes depend on not only solar radiation but also scattering. This extra controlling factor can lead to lower correlations. Especially, since the collision cross section is proportional to the reverse of energy square ($1/E^2$)

[*Rutherford*, 1911; *Khazanov and Liemohn*, 1995], high-energy photoelectrons are harder to be scattered into the trapped zone. This may also be the reason for the different behaviors within the trapped zone for low and high energies. In addition, *Liemohn et al.* [2003] noted that observed high-energy photoelectron pitch angle distributions were more isotropic than at lower energies, indicating other scattering mechanisms could be dominant (e.g., wave-particle interactions).

After multiplying time-history dust opacities as new controlling functions, as shown in Figure 6 (bottom), a similar pattern to Figure 6 (top) is found, but the correlation now is much higher in most bins. Especially, the number now is above 0.8 for the lower energies across all pitch angles. The obvious increases in the source region of high energies are also seen. However, as mentioned above, lower correlations than with the EUV proxy only are seen in the trapped zone of high-energy channels.

As said above, it is important that the correlation after including the time-history dust opacities is higher than the correlation with the local EUV proxy only. To further demonstrate this criteria, the quantitative difference of Figure 6 (top and bottom) is shown in Figure 7, both the absolute and relative difference given in the two panels, respectively. For energy below 53 eV, the increase of correlation is mostly above 0.1, up to 0.25. Also, it appears that the downward fluxes experience a higher increase than do the upward fluxes while the trapped zone seems to be the lowest, again. For energy above 53 eV, the increase of correlations in the 115 eV and 190 eV channels, both displaying a double linear trend in the scatterplots, is seen across all the pitch angles, above 0.1 in the source region. For the 61 eV and 79 eV energy channels, there was barely flux separation seen in the scatterplots of electron fluxes against local EUV proxy but there is seen a correlation improvement in the source region, as shown in Figure 6. It implies that the disappearance of the double linear trend in these two energy channels might be due to spacecraft potential effects that mix the very
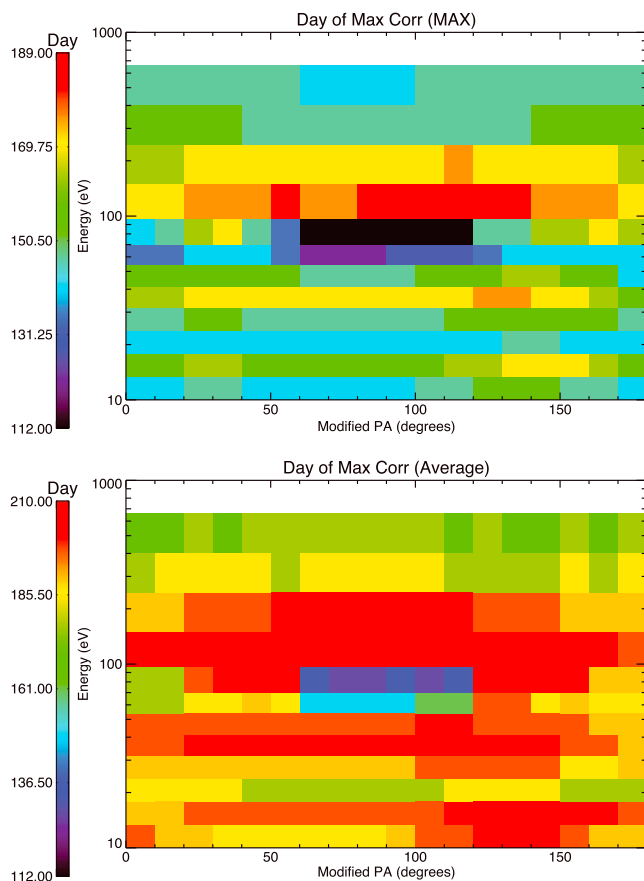
Figure 8. The time window lengths of the transition points in Figure 5 for the maximum-value/running-average (top/bottom, respectively) time-history dust opacity method. Note that the color scales of the two are different.
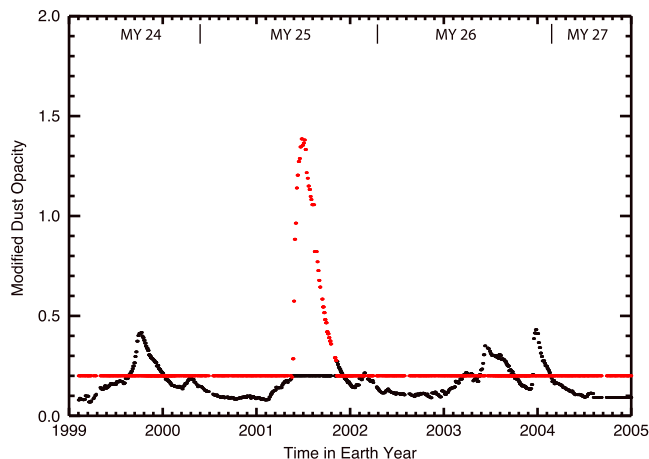

Figure 9. Two sets of modified dust opacities versus time. The red (black) line is for the high (low) dust case.

different flux intensities above and below the knee in these bins rather than some physical processes. Finally, the two highest examined energy channels, 313 eV and 515 eV, only have small increases (of less than 0.1) at a few source region bins. Over all, an increase of correlation in the source region is the common feature of high energies. While excluding two channels near the knee, it seems that the increase in the trapped zone is less and less when energy increases. The relative difference of the before/after including time-history dust opacities is also given in Figure 7 (bottom). The pattern resembles the absolute difference plot. Mostly, the increase of correlation is around 20%. In all, it appears that when there is a flux separation in the scatterplots like Figure 4, the correlation coefficient after including the time-history dust opacities will also more or less improve, such as for all the pitch angles of low energies and in the source region of high energies; on the contrary, when there is barely flux separation, little improvement is seen, like the trapped zone of high energies. The general improvement of correlations at all energies suggests that dust storms are responsible for the appearance of the second linear trend.

The fact that the maximum increase of correlation happens with ≥ 100 Earth day time-history dust opacities instead of instantaneous opacity values suggests a long-lasting effect of dust storms, as claimed by *Liemohn et al.* [2012]. The exact time length of this long-lasting effect is also significant, shown in Figure 8, determined according to the method said above, Figure 8 (top and bottom) corresponding to the maximum value and running average methods, respectively. Also, notice that only for those bins with significant correlation improvement is the time-window length significant. For the maximum value case, this time length for low
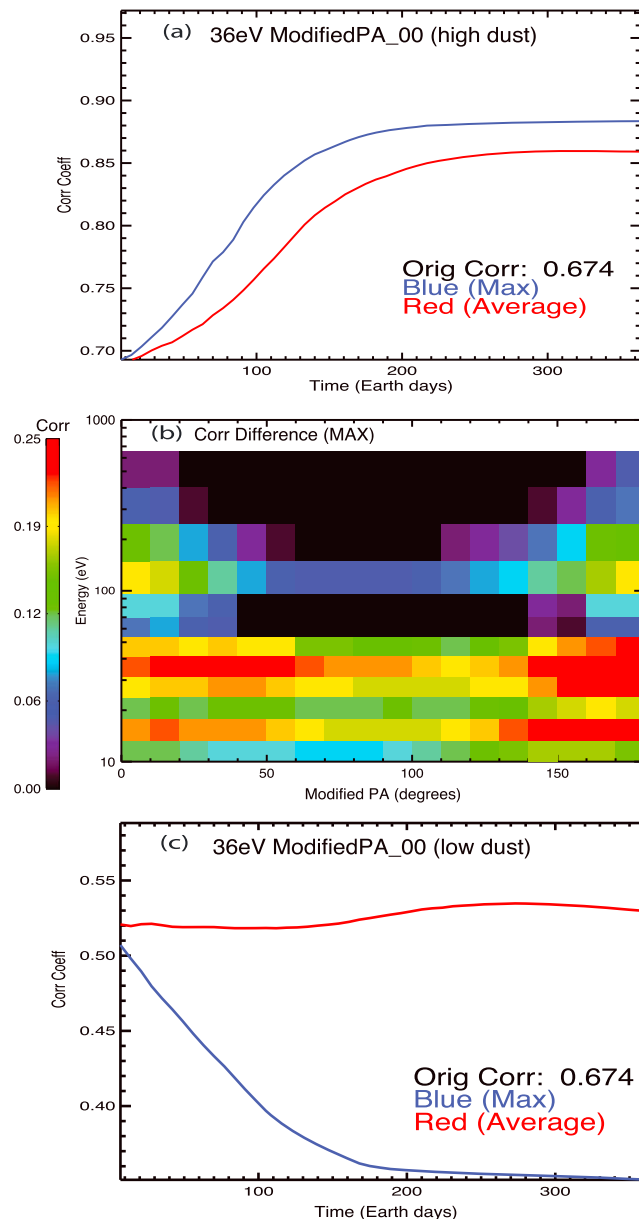
Figure 10. (a) Correlation coefficients of the fluxes of 36 eV photoelectrons at PA 0°–10° versus the window length of the time-history dust opacities for the high dust case. Again, "Orig Corr" denotes the correlation without the inclusion of dust opacities. (b) The absolute correlation difference of all the energy and pitch angle bins between before and after including the time-history dust opacities for the high dust case. (c) Correlation coefficients of the fluxes of 36 eV photoelectrons at PA 0°–10° versus the window length of the time-history dust opacities for the low dust case. Red (blue) curve in Figures 10a and 10c highlights the running-average (maximum value) dust opacity method. Also, notice that the *y* axes have different ranges for the two plots.

energies is around 140–160 Earth days (approximately 70°–84° Ls at Mars, given 1° Ls is about 1.9 Earth days on average at Mars) while for a few high-energy bins where dust storms seem to play a role, the influence lasts longer, up to almost 190 Earth days (approximately 100° Ls at Mars). By comparing Figures 7 (top) and 8 (top), an interesting feature is seen, for low energies, the history window seems longer where the increase of correlation is higher. For the running average case, the time length is around 210 Earth days (approximately 110° Ls at Mars) for most bins. Notice that the time-history length of the maximum value case is different from *Liemohn et al.* [2012] (which said 210 Earth days for both cases). It is because the method of determining this window length is different between the two studies. In fact, both studies have an agreement that the influence of dust storms is long-lasting instead of an instantaneous effect.

3.2. Relationship With Modified Dust Opacity Levels

The results above have shown that the conclusion of dust storms' long-living influence on photoelectrons applies to all energy and pitch angle bins below 53 eV and also the source region of higher energies. However, large dust storms occurred on Mars in every southern spring from MY 24–27, as shown in Figure 3b. It is not yet clear whether all the dust storms affect the photoelectrons or whether the global-scale dust storm at MY 25 is special. Hence, two sets of modified dust opacity are made, by isolating the dust storm at MY 25 from the rest of the timeline. The first artificial dust opacity time series is the dust storm MY 25 opacity with a constant 0.2 for the rest of the time, colored as red in Figure 9

(denoted as high dust opacity) while the second new dust time series has the original low dust opacity everywhere but substitutes the large dust storm with a constant 0.2 level, colored black in Figure 9 (denoted as low dust opacity). The same time-history method has been applied to both sets, and the results are shown in Figures 10a and 10b corresponding to high dust opacity and Figure 10c to low dust opacity.

Figure 10a shows an example of the plot of *R* against history-time window of 36 eV at pitch angle 0°–10°, and red and blue highlight the two methods of time-history dust opacity calculation, maximum and average. Similar to Figure 5, the correlation increases first and then levels off as the window length increases. In fact, the other line plots of this high dust opacity case resemble the real case. To illustrate this, the absolute difference of two sets of correlation coefficients, before and after including dust opacity, is given in Figure 10b. Compared with Figure 7 (top), the two plots appear to be almost the same, with an increase of correlation seen in all the pitch angles of low energies and in the source region of high energies. This similarity between these two cases implies that the dust storm in MY 25 is entirely responsible for the improvement of correlation as well as the merging of the double linear trend in scatterplots.

To further investigate the influence of the unusually large dust storm, correlations for the low dust opacity case have also been conducted. One example of this low dust opacity case is exhibited in Figure 10c, the plot of *R* against time-history window for 36 eV at pitch angle 0°–10° (as was shown in Figure 10a for the high dust case). The line shape no longer keeps increasing, but decreasing for the blue line. Also, the correlation coefficient with EUV proxy only is 0.67, given in the right lower corner, while the correlation after multiplying dust opacity is always lower than 0.55. Similarly, all the examined energy and pitch angle bins share the same feature that the inclusion of low dust opacity actually diminishes the correlation coefficients.

The opposite results for the two artificial dust opacity profiles strongly suggest not only that the dust storm in MY 25 is entirely responsible for the second linear trend in the scatterplots but also that the usual dust storms have little influence on photoelectrons. It appears that dust storms with high 9 μm dust optical depths (τ greater than a certain value between 0.5 and 1.4) can significantly change the Martian upper atmosphere.

4. Discussion

The results presented above show that dust in the lower atmosphere has a long-lasting influence on high-altitude photoelectron fluxes. Note that photoelectrons will recombine and be lost to the neutral atmosphere on the nightside; thus, such a long-living effect of dust storm must be due to the changes in the neutral atmosphere [*Liemohn et al.*, 2012]. Two highly possible candidates of how dust storms affect the photoelectron fluxes are the change in the source, e.g., the perturbation of the neutral density below 400 km, and/or high-altitude scattering due to the density change at or above the altitude of MGS. With the inclusion of time-history dust opacities, a significant increase of correlation between photoelectron fluxes and the new controlling function is seen at all the low-energy bins and more field-aligned high-energy bins but not the trapped zone of high-energy channels. As mentioned in the section 2, the source region pitch angles are more directly related to the source at the ionosphere while the trapped zone is more influenced by high-altitude scattering. The increase of correlation happens at the source region of all energies, suggesting that the effects of dust storms more likely happen in the ionosphere. The different behaviors of trapped zones of different energy channels, again, can be caused by the fact that the collision cross section is proportional to the inverse of energy squared ($1/E^2$). Low-energy photoelectrons are more easily scattered into the trapped zone. In other words, the low-energy trapped zone is more sensitive to changes of sources than the high-energy trapped zone. In contrast, even if high-energy photoelectron fluxes in the ionosphere change due to dust storms, it might not be shown in the trapped zone at 400 km. In fact, before relating dust storms, the flux separation in the scatterplot of photoelectron flux against EUV proxy is found in both source and trapped pitch angles. It already implicates that driving processes more likely happen in the source cone as the photoelectrons in the trapped pitch angles are less likely to affect those in the source regions.

Therefore, the results imply changes to the neutral densities in the thermosphere rather than the exosphere. According to Chapman production function [*Schunk and Nagy*, 2009, equation 9.21], the peak production rate occurs at unit optical depth and is directly proportional to the neutral density at the bottomside of the thermosphere [*Schunk and Nagy*, 2009, equation 11.55]. The additional solar energy absorption of dust particles heats the lower atmosphere and therefore results in a larger-scale height at low altitudes, which leads to an enhanced neutral density at the bottom of the thermosphere. This will then increase the peak production rate of photoelectrons. Note that ER measures the nonthermal primary photoelectrons (>10 eV), as opposed to the thermal electrons that dominate the main peak and participate in the equilibrium that establishes the Chapman-like structure. The fluxes of nonthermal primary photoelectrons detected by ER are determined by not only the source but also the loss due to scattering. The elevated neutral density at

the bottom of the thermosphere can increase both, and our results suggest that the change in the source is greater than the loss. However, a more rigorous and quantitative explanation requires modeling, which is planned as future work.

The artificial opacity time series case has shown that only the dust storm at MY 25 is able to significantly affect photoelectron fluxes. It appears that dust storms with high 9 μm dust optical depths can significantly change the Martian upper atmosphere. In fact, although *Lillis et al.* [2010b] concluded that there was no clear trend between total electron content (TEC) in the Mars ionosphere and dust opacity, there was indeed a sudden increase of TEC at the end of MY 28, corresponding to the time period of a dust storm that reached a 9 μm dust optical depth of 1.0. The dust opacities are obtained from the Thermal Emission Imaging System (THEMIS) [e.g., *Smith*, 2009]. Despite that the peak of dust opacity seemed broader than peaks of TEC, *Lillis et al.* [2010b] did not rule out the connection between the two, given no apparent change of other drivers. Our results imply that it is the changes in the ionosphere caused by the global-scale dust storm at MY 25 that greatly modified photoelectron fluxes at 400 km while this increase of TEC also shows the changes at ionospheric altitudes potentially caused by the global-scale dust storm at MY 28. However, it is not yet clear whether the influence of the global-scale dust storm at MY 28 on the ionosphere is long-lasting or not. Therefore, it is necessary to analyze the electron data from Mars Express ASPERA-3 ELS [e.g., *Barabash et al.*, 2006] and apply the similar method to investigate the time-history effects of the dust storm at MY 28 on electron fluxes. If it turns out that the MY 28 dust storm does not have a obvious and/or long-lasting effect on photoelectron fluxes and the ionosphere, it might imply that the MY 25 dust storm was special in some way and was a one-time event. And if the MY 28 dust storm does have an obvious and/or long-lasting influence, together with our results, it suggests that there exists a dust opacity threshold above which dust storms cause obvious and/or long-lasting changes in the ionosphere, or even higher altitudes like 400 km, exists. Given the dust opacity values from Mars year 24 to 28 [e.g., *Smith*, 2006, 2009; *Medvedev et al.*, 2011], this threshold might be roughly between a global-averaged 9 μm dust optical depth, τ, of 0.5 and 1.0. In other words, as long as dust storms become large enough, above this threshold, they are able to affect the entire atmosphere to such an extent that the ionosphere and photoelectron fluxes are significantly affected.

Since we only investigated one case (MY 25 dust storm), it is hard to characterize the nature of the link between the dust storms and photoelectron fluxes and the ionosphere. The globally averaged 9 μm dust optical depth threshold could lead to many possibilities for the underlying physics. For example, on one hand, the dust threshold could be related to the height where dust is still dense enough to significantly alter the upper atmosphere. On the other hand, global-scale dust storms might change the circulation or state of the lower atmosphere in ways that are transmitted to the upper atmosphere. It is also very possible that the two scenarios are connected. All these possibilities not only indicate the complex interactions between physical processes but also demand further investigation of this issue.

Both *Liemohn et al.* [2012] and our study have shown that dust storms' influence tends to be long-lived, as long as about 140–160 Earth days (approximately 70°–84° Ls at Mars). This influence may be due to a long-lasting thermospheric density increase caused by dust storms. In fact, *Withers and Pratt* [2013] claimed a corrected decay time, approximately 80°–120° Ls, of neutral density enhancement at altitudes of 130–160 km. The upper atmospheric changes by dust storms can also remain longer than the decay of the dust storms themselves, about 32° Ls, by analyzing the atmospheric densities at northern latitudes (30°–60°N) from the MGS accelerometer responding to the Noachis dust storm (40°S, 20°E). In other words, the atmospheric densities remained elevated even though dust opacities dropped back to their prestorm level. However, the correction to the neutral density decay time removes the effects of changing latitude and changing season, while the latter should be considered in our case since in reality density did decrease when the season advanced into winter. Hence, the fitted decay timescales (τ_{fit}), given in both Ls degrees and approximate Earth days, are examined again here, shown in Table 1 (values from Table 1 of *Withers and Pratt* [2013]). Outbound measurements of latitudes from 30°N to 40°N, closer to the place where the dust storm originated, have longer fitted decay times, above 50° Ls and up to 80° Ls at the most equatorward latitude (corresponding to 100–160 Earth days), than the inbound measurements at latitudes greater than 40°N (where decay time is approximately 80–100 Earth days). The fact that an 80° Ls decay of atmospheric density responds to a dust storm with a peak localized 9 μm dust opacity $\tau \sim 0.75$ with a decay time of 32° Ls hints that dust storms' effects on regional atmospheric densities can last longer than the dust storm itself. Our study shows that the time length of the long-lasting effects of the global dust storm with a peak globally averaged 9 μm dust opacity $\tau \sim 1.5$ in MY 25, about 140–160 Earth days, is roughly the same time

Table 1. [a]Atmospheric Densities Measured by the MGS Accelerometer During the Noachis Dust Storm and Related Properties[b]

Altitude (km)	Direction	Latitude (°N)	τ_{fit} (deg)	τ_{fit} (Earth Days)
130	Outbound	32.6–39.1	53.31 ± 4.53	101.3 ± 8.6
140	Outbound	32.2–36.4	59.65 ± 3.95	113.3 ± 7.5
150	Outbound	29.5–34.4	73.12 ± 4.98	138.9 ± 9.5
160	Outbound	27.5–32.6	82.98 ± 6.50	157.7 ± 12.6
130	Inbound	43.1–51.8	42.93 ± 2.78	81.6 ± 5.3
140	Inbound	44.2–54.5	39.64 ± 1.72	75.3 ± 3.3
150	Inbound	46.9–56.5	41.65 ± 1.98	79.1 ± 3.8
160	Inbound	49.0–58.3	50.94 ± 3.24	96.8 ± 6.2

[a]Values from Table 1 of *Withers and Pratt* [2013].

[b]The latitude range reported for each set of measurements corresponds from Ls = 224° to Ls = 260°. τ_{fit} is the decay timescale obtained by a direct exponential fit to the data, given in both Ls degrees and approximate Earth days. The uncertainties are 1σ.

length of the dust storm itself. In other words, the response of photoelectron fluxes lasts approximately twice long as the dust storm, which matches the analysis above.

Another possibility is the influence of the two persistent high-altitude dust layers, centered at 20–30 km, high-altitude tropical dust maximum (HATDM), and 45–65 km, upper dust maximum (UDM) [*Guzewich et al.*, 2013]. Given very few dust retrievals above 60 km, *Guzewich et al.* [2013] did not exclude the possibility of the UDM being located at altitudes higher than 60 km, especially during the MY 25 global dust storm. These two high-altitude dust layers may influence the neutral atmosphere, thus the photoelectron fluxes, at altitudes higher than we originally assumed. Even though dust storms contribute to these two dust layers, they are not usually the determinant factor. It is possible that a change in these two layers due to a dust storm lasts longer than the transient dust storm itself. The changes experienced by these two layers, especially the UDM, could be transmitted into the thermosphere/ionosphere. However, it is also important to notice that these two dust layers are a detail within the main column of dust and therefore less likely to be a candidate causing significant changes in the upper atmosphere.

In addition, *Forbes et al.* [2008] has shown that the MGS neutral densities at 400 km and exospheric temperatures are fit well (correlation coefficients of 0.96 and 0.99, respectively) with a Mars-adjusted $F_{10.7}$ and an additional seasonal term, without any additional augmentation from a dust term. It suggests that dust storms do not cause a long-lasting effect on the exosphere. It may explain why there is no obvious improvement of correlation after adding time-history dust opacities at the trapped pitch angles, which is mainly affected by the state of the neutral exosphere.

One possible error of the results of high-energy photoelectron is to use an EUV proxy based on $F_{10.7}$. Hence, another EUV proxy based on the Flare Irradiance Spectral Model (FISM) [*Chamberlin et al.*, 2007, 2008] with the same interpolation from Earth to Mars is employed to repeat the procedure above. The EUV irradiance is integrated over several bandwidths (0–10 nm, 0–50 nm, and 50–100 nm) to obtain the solar EUV fluxes. It turns out that the all the results are nearly identical with the EUV proxy based on $F_{10.7}$ (included in Figures S1–S3 in the supporting information accompanying this paper). It suggests that the difference between the proxy based on $F_{10.7}$ and FISM is small and that the possible error from interpolation from Earth to Mars is more dominant. Regardless, even for high-energy photoelectrons, the correlation of their fluxes and these solar EUV proxies is greater than 0.5 for source pitch angles, decent enough to make the case.

Another possible error may result from the contamination of spacecraft secondary electrons at high-energy channels [*Furman and Pivi*, 2003]. The contamination filter, excluding anode sections 5–12 facing the spacecraft, is also applied to high-energy channels. This new set of results are also nearly identical to those presented in section 3 (included in Figure S4 in the supporting information accompanying this paper). It implies that the possible contamination at high-energy channels seems insignificant to our study.

5. Conclusions

A survey of the Mars Global Surveyor electron data across all the pitch angles (PAs) of 12 usable energy bins (11 eV–746 eV) for dayside photoelectron observations over regions of strong crustal fields was conducted. The results have shown that the unusual bimodal solar flux dependence of dayside photoelectron fluxes is seen in all the pitch angles of low energies (≤ 53 eV) and some bins of higher-energy channels but is not obvious in the rest of high-energy bins. By applying time-history dust opacities to obtain new controlling functions, the separations seen in the scatterplots are now merged into one linear trend. In addition, quantitatively, obvious correlation coefficient increases are also found at all pitch angles of energy channels lower than 53 eV and source regions of higher-energy channels, even for 61 eV and 79 eV, two channels that are near the knee of the photoelectron energy spectrum.

The results not only confirm that dust storms' influence on photoelectron fluxes are long-lasting, about 140–160 Earth days (approximately 70°–84° Ls at Mars), but also imply that the changes caused by dust storms are most likely occurring in the source region, i.e., the thermosphere/ionosphere. Furthermore, the isolation of the global dust storm at MY 25 from the rest of dust opacities shows that this global-scale dust storm is entirely responsible for photoelectron fluxes' second solar flux-dependent trend. While it is possible that the MY 25 global dust storm was a one-time event, based on the results of this paper and *Lillis et al.* [2010b], we hypothesize that if the global-averaged 9 μm dust optical depth, τ, exceeds a threshold between 0.5 and 1.0, dust storms are more likely to cause significant and/or long-lasting changes in photoelectron fluxes and the ionosphere.

Two possible explanations as to why dust storms have such long-living effects are also given. First, the atmospheric density decay time could be much longer than the dust storm decay time. Such long-term elevated atmospheric densities can significantly increase the photoelectron fluxes at MGS altitude for a very long time. In addition, two high-altitude dust layers, HATDM and UDM, might affect the thermosphere/ionosphere more than transient dust storms as they are located at higher altitudes, and the changes of these two layers caused by dust storms might linger longer after dust storms subside.

6. Future Work

To further examine this connection, it is necessary to analyze the atmospheric temperature profiles from TES and study how long the neutral atmosphere remained inflated in response to the dust storm. Also, in the section 4, we have discussed the importance to investigate how the global dust storm at MY 28 affects the photoelectron fluxes by analyzing the electron data from Mars Express ASPERA-3 ELS [e.g., *Barabash et al.*, 2006], combined with the dust opacity values from THEMIS [e.g., *Smith*, 2009]. However, the lack of a magnetometer on Mars Express complicates the interpretation of these measurements with respect to photoelectrons on closed magnetic loops. In addition, a superthermal electron transportation model [e.g., *Liemohn et al.*, 2003, 2006] can be used to study how the photoelectron fluxes respond to different neutral atmospheres with different dust opacities. Finally, it is also important to use Martian thermosphere models [e.g., *Bougher et al.*, 2006], even coupled with lower Martian atmosphere models, to study how the dust storms affect the upper atmosphere, hence the high-altitude photoelectron fluxes.

References

Acuña, M., et al. (1992), Mars observer magnetic fields investigation, *J. Geophys. Res.*, *97*(E5), 7799–7814.

Baird, D. T., R. H. Tolson, S. Bougher, and B. Steers (2007), Zonal wind calculations from Mars global surveyor accelerometer and rate data, *J. Spacecr. Rockets*, *44*(6), 1180–1187.

Barabash, S., et al. (2006), The analyzer of space plasmas and energetic atoms (ASPERA-3) for the Mars express mission, *Space Sci. Rev.*, *126*(1-4), 113–164.

Bell, J. M., S. W. Bougher, and J. R. Murphy (2007), Vertical dust mixing and the interannual variations in the Mars thermosphere, *J. Geophys. Res.*, *112*, E12002, doi:10.1029/2006JE002856.

Bougher, S., J. Murphy, and R. Haberle (1997), Dust storm impacts on the Mars upper atmosphere, *Adv. Space Res.*, *19*(8), 1255–1260.

Bougher, S., G. Keating, R. Zurek, J. Murphy, R. Haberle, J. Hollingsworth, and R. Clancy (1999), Mars Global Surveyor aerobraking: Atmospheric trends and model interpretation, *Adv. Space Res.*, *23*(11), 1887–1897.

Bougher, S. W., S. Engel, D. Hinson, and J. Murphy (2004), MGS radio science electron density profiles: Interannual variability and implications for the Martian neutral atmosphere, *J. Geophys. Res.*, *109*, E03010, doi:10.1029/2003JE002154.

Bougher, S., J. Bell, J. Murphy, M. Lopez-Valverde, and P. Withers (2006), Polar warming in the Mars thermosphere: Seasonal variations owing to changing insolation and dust distributions, *Geophys. Res. Lett.*, *33*, L02203, doi:10.1029/2005GL024059.

Chamberlin, P. C., T. N. Woods, and F. G. Eparvier (2007), Flare Irradiance Spectral Model (FISM): Daily component algorithms and results, *Space Weather*, *5*, S07005, doi:10.1029/2007SW000316.

Chamberlin, P. C., T. N. Woods, and F. G. Eparvier (2008), Flare Irradiance Spectral Model (FISM): Flare component algorithms and results, *Space Weather*, *6*, S05001, doi:10.1029/2007SW000372.

Christensen, P. R., et al. (1992), Thermal emission spectrometer experiment: Mars Observer mission, *J. Geophys. Res.*, *97*(E5), 7719–7734.

Christensen, P. R., et al. (2001), Mars Global Surveyor Thermal Emission Spectrometer experiment: Investigation description and surface science results, *J. Geophys. Res.*, *106*(E10), 23,823–23,871.

Clancy, R. T., M. J. Wolff, B. A. Whitney, B. A. Cantor, M. D. Smith, and T. H. McConnochie (2010), Extension of atmospheric dust loading to high altitudes during the 2001 Mars dust storm: MGS TES limb observations, *Icarus*, *207*(1), 98–109.

England, S. L., and R. J. Lillis (2012), On the nature of the variability of the Martian thermospheric mass density: Results from electron reflectometry with Mars Global Surveyor, *J. Geophys. Res.*, *117*, E02008, doi:10.1029/2011JE003998.

Forbes, J. M., F. G. Lemoine, S. L. Bruinsma, M. D. Smith, and X. Zhang (2008), Solar flux variability of Mars' exosphere densities and temperatures, *Geophys. Res. Lett.*, *35*, L01201, doi:10.1029/2007GL031904.

Furman, M., and M. Pivi (2003), Simulation of secondary electron emission based on a phenomenological probabilistic model, Lawrence Berkeley National Laboratory. [Available at http://escholarship.org/uc/item/5dj265n8.]

Gierasch, P. J., and R. M. Goody (1972), The effect of dust on the temperature of the Martian atmosphere, *J. Atmos. Sci.*, *29*, 400–402, doi:10.1175/1520-0469(1972).

Guzewich, S. D., E. R. Talaat, A. D. Toigo, D. W. Waugh, and T. H. McConnochie (2013), High-altitude dust layers on Mars: Observations with the thermal emission spectrometer, *J. Geophys. Res. Planets*, *118*, 1177–1194, doi:10.1002/jgre.20076.

Haberle, R. M., C. B. Leovy, and J. B. Pollack (1982), Some effects of global dust storms on the atmospheric circulation of Mars, *Icarus*, *50*(2), 322–367.

Hantsch, M., and S. Bauer (1990), Solar control of the Mars ionosphere, *Planet. Space Sci.*, *38*(4), 539–542.

Keating, G., et al. (1998), The structure of the upper atmosphere of Mars: In situ accelerometer measurements from Mars Global Surveyor, *Science*, *279*(5357), 1672–1676.

Khazanov, G., and M. Liemohn (1995), Nonsteady state ionosphere-plasmasphere coupling of superthermal electrons, *J. Geophys. Res.*, *100*(A6), 9669–9681.

Liemohn, M. W., D. L. Mitchell, A. F. Nagy, J. L. Fox, T. W. Reimer, and Y. Ma (2003), Comparisons of electron fluxes measured in the crustal fields at Mars by the MGS magnetometer/electron reflectometer instrument with a B field-dependent transport code, *J. Geophys. Res.*, *108*(E12), 5134, doi:10.1029/2003JE002158.

Liemohn, M. W., et al. (2006), Numerical interpretation of high-altitude photoelectron observations, *Icarus*, *182*(2), 383–395.

Liemohn, M. W., A. Dupre, S. W. Bougher, M. Trantham, D. L. Mitchell, and M. D. Smith (2012), Time-history influence of global dust storms on the upper atmosphere at Mars, *Geophys. Res. Lett.*, *39*, L11201, doi:10.1029/2012GL051994.

Lillis, R. J., S. W. Bougher, D. L. Mitchell, D. A. Brain, R. P. Lin, and M. H. Acuña (2008), Continuous monitoring of nightside upper thermospheric mass densities in the Martian southern hemisphere over 4 Martian years using electron reflectometry, *Icarus*, *194*(2), 562–574.

Lillis, R. J., S. W. Bougher, F. González-Galindo, F. Forget, M. D. Smith, and P. C. Chamberlin (2010a), Four Martian years of nightside upper thermospheric mass densities derived from electron reflectometry: Method extension and comparison with GCM simulations, *J. Geophys. Res.*, *115*, E07014, doi:10.1029/2009JE003529.

Lillis, R. J., D. A. Brain, S. L. England, P. Withers, M. O. Fillingim, and A. Safaeinili (2010b), Total electron content in the Mars ionosphere: Temporal studies and dependence on solar EUV flux, *J. Geophys. Res.*, *115*, A11314, doi:10.1029/2010JA015698.

Medvedev, A. S., T. Kuroda, and P. Hartogh (2011), Influence of dust on the dynamics of the Martian atmosphere above the first scale height, *Aeolian Res.*, *3*(2), 145–156.

Mitchell, D., R. Lin, C. Mazelle, H. Reme, P. Cloutier, J. Connerney, M. Acuña, and N. Ness (2001), Probing Mars' crustal magnetic field and ionosphere with the MGS electron reflectometer, *J. Geophys. Res.*, *106*(E10), 23,419–23,427.

Rutherford, E. (1911), The scattering of α and β particles by matter and the structure of the atom, *Philos. Mag.*, *21*, 669–688.

Schunk, R., and A. Nagy (2009), *Ionospheres: Physics, Plasma Physics, and Chemistry*, 2nd ed., 628 pp., Cambridge Univ. Press, Cambridge, U. K.

Smith, M. D., B. J. Conrath, J. C. Pearl, and P. R. Christensen (2002), Thermal Emission Spectrometer observations of Martian planet-encircling dust storm 2001a, *Icarus*, *157*(1), 259–263.

Smith, M. D. (2004), Interannual variability in TES atmospheric observations of Mars during 1999–2003, *Icarus*, *167*(1), 148–165.

Smith, M. (2006), TES atmospheric temperature, aerosol optical depth, and water vapor observations 1999–2004, in *The Second Workshop on Mars Atmosphere Modelling and Observations*, edited by F. Forget et al., 211 pp., IAA, Granada, Spain.

Smith, M. D. (2009), THEMIS observations of Mars aerosol optical depth from 2002–2008, *Icarus*, *202*(2), 444–452.

Tracadas, P. W., M. T. Zuber, D. E. Smith, and F. G. Lemoine (2001), Density structure of the upper thermosphere of Mars from measurements of air drag on the Mars global surveyor spacecraft, *J. Geophys. Res.*, *106*(E10), 23,349–23,357.

Trantham, M., M. Liemohn, D. Mitchell, and J. Frank (2011), Photoelectrons on closed crustal field lines at Mars, *J. Geophys. Res.*, *116*, A07311, doi:10.1029/2010JA016231.

Wang, J.-S., and E. Nielsen (2003), Behavior of the Martian dayside electron density peak during global dust storms, *Planet. Space Sci.*, *51*(4), 329–338.

Withers, P., and R. Pratt (2013), An observational study of the response of the upper atmosphere of Mars to lower atmospheric dust storms, *Icarus*, *225*, 378–389.

Zou, H., R. J. Lillis, J. S. Wang, and E. Nielsen (2011), Determination of seasonal variations in the Martian neutral atmosphere from observations of ionospheric peak height, *J. Geophys. Res.*, *116*, E09004, doi:10.1029/2011JE003833.